Local isotropy test based on the oriented perimeter of digitalized images

Mariem Abaach, Hermine Biermé, Elena Di Bernardino, Anne Estrade

Local isotropy test based on the oriented perimeter of digitalized images

Mariem Abaach
Université Paris Cité, CNRS, UMR 8145, MAP5, Paris, France,
e-mail: mariem.abaach@u-paris.fr

Hermine Biermé
Université de Tours, CNRS, UMR 7013, IDP, France,
e-mail: hermine.bierme@univ-tours.fr

Elena Di Bernardino
Université Côte d'Azur, CNRS UMR 7351, Laboratoire J.A. Dieudonné, France,
e-mail: Elena.Di_bernardino@unice.fr

Anne Estrade *
Université Paris Cité, CNRS, UMR 8145, MAP5, Paris, France,
e-mail: anne.estrade@u-paris.fr

March 20, 2023

Abstract

In this paper we consider the oriented perimeter of a thresholded grey-level image. This geometrical quantity is built by considering separately the horizontal and vertical contributions of the pixel. We explicitly compute the first two moments of the so-called oriented perimeter under the hypothesis of an underlying discrete Gaussian stationary field. We establish a Central Limit Theorem, as the number of pixels goes to infinity, for the joint oriented perimeters at various levels under a summability condition of the covariance function. By using the CLT previously established, we then construct a consistent local isotropy test, based on the ratio of the oriented perimeters. Our theoretical study is completed by extensive numerical illustrations based on simulated data. Finally, we apply our method to detect local isotropy in calcaneus X-ray images.

Keywords: Central Limit Theorem, Discrete geometry, Excursion sets, Gaussian fields, Geometric statistics, Medical imaging

*The authors gratefully acknowledge the French government, through the project ANR MISTIC (ANR-19-CE40-0005) and the 3IA Côte d'Azur Investments in the Future project managed by the National Research Agency (ANR) with the reference number ANR-19-P3IA-0002.

1 Introduction

The main objective of our study is to be able to decide whether the texture of a grey-level image is isotropic or not. By the texture of an image, we mean the microscopic structure that is captured by the covariance function at the pixels scale. In order to achieve this goal, we propose a methodology built on a statistical test for which all steps are rigorously validated. The originality of our approach is to stick on the geometrical features of the image without trying to identify the full distribution of the underlying Gaussian random field that is supposed to serve as a model. More precisely, our observable statistic will be the perimeter of the black domain of the thresholded image.

In the previous literature, a number of non-parametric tests of directional dependence have been developed using both the spatial and spectral representations of random fields (see, e.g, Weller and Hoeting [2016], Guan et al. [2004]). A comparative study with these methods is proposed in Appendix E. The present paper is part of the methodological literature that deals with statistical inference based on geometrical observable features given by the Lipschitz-Killing curvatures (LKC) of the excursion sets. In image analysis, *i.e.* in a two dimensional setting, an excursion set is a region of the image where the pixel's values are higher than a fixed level, the level set is the boundary of the excursion set and the LKC's are the three natural Minkowski functionals: Euler characteristic (number of connected components minus number of holes), perimeter (length of the level set), area (Lebesgue measure of the excursion set). Although such type of statistical study of the excursion set is an old engineers task (see Longuet-Higgins [1957] for instance), it has recently received much attention from a probability theory and mathematical statistics point of view. To cite some of these papers, let us quote Worsley [1996] or Telschow et al. [2020] where the localization of peaks is infered from the observation of the Euler characteristic of excursion sets in neuroimaging and in the cosmic background radiation, Molina and Feito [2002] where isotropy is tested through the observation of the gradient, Di Bernardino et al. [2017] or Biermé et al. [2019] where a test of Gaussianity is produced based on the Euler characteristic of excursion sets, Abaach et al. [2021] where a test of symmetry is produced based on the perimeter of thresholded images. Among this dense literature, let us focus on two specific articles, Cabaña [1987], Berzin [2021], with a similar objective as ours, namely a test of isotropy, based on similar observations, namely the

length of level sets. Both papers are concerned with affine two-dimensional continuous random fields, *i.e.* stationary random fields X defined on $\mathbb{R}^2$ and given as $X(\cdot) = Z(A\cdot)$, where Z is centered, stationary and isotropic defined on $\mathbb{R}^2$ and A is a deterministic matrix that can be reduced to $A = \begin{pmatrix} a & 0 \\ 0 & b \end{pmatrix} \begin{pmatrix} \cos\theta & \sin\theta \\ -\sin\theta & \cos\theta \end{pmatrix}$, $a, b \in \mathbb{R}$, $\theta \in (0, 2\pi)$. Within this continuous parametric frame, X is isotropic in distribution if and only if $a = b$. In both articles, a test of isotropy is constructed, based on the measurement of the respective horizontal and vertical components of the length of the level sets. In the former article, some mixing condition yields a Gaussian asymptotics of the normalized level set length, while in the later article, a Gaussian condition yields a similar result. This central limit theorem is the crux for establishing a fair statistical test. Let us insist on the continuous setting that is assumed in those papers whereas our study definitively deals with discrete images. Our precise setting will be presented later on in the introductory section.

Implementations of this type of "geometrical" methods can be found in medical imaging and image analysis in general, cosmology, hydrology, sea waves modeling, etc. As an example, let us exhibit some medical images that can be handled with our methodology. In this introductory part, we just show the images and a first tentative of descriptive statistics. The statistical results that we are able to infer from our methodology is detailed at the end of the present paper (see Section 5). We analyzed 211 X-ray images of calcaneus bones in order to detect the eventual anisotropic nature of the microarchitecture since bone texture anisotropy is of special interest for the diagnosis of osteoporosis (see Chappard et al. [2005] for instance or Wani and Arora [2020] for a review). We first applied a preprocessing step in order to get stationary images and then consider the thresholded images at various empirical quantile levels t_α, *i.e.* for $\alpha \in (0, 1)$, there exists a proportion α of the image values smaller than t_α.

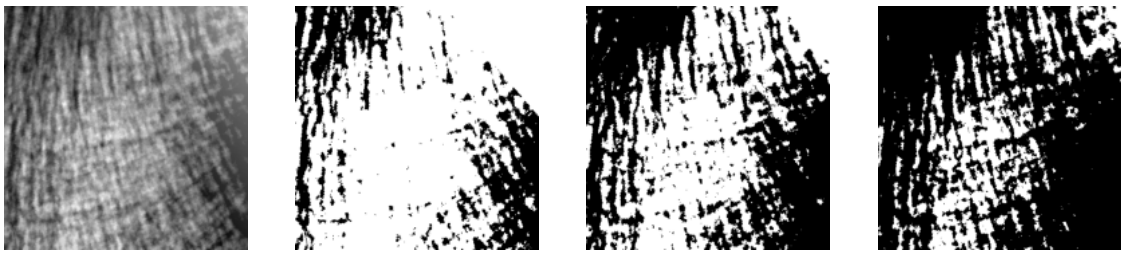

Figure 1: Stationnarized bone X-ray image, with its associated excursion sets thresholded at the first, second and third quartile.

As observable statistics, we use the respective numbers of horizontal and vertical edges that separate a black pixel from a white pixel of the binary image. We name these counters as oriented perimeters, horizontal and vertical respectively. In case of an isotropic texture, the ratio of the two oriented perimeters should be close to one. At the opposite, if the observed ratio is far from one, then some anisotropy is expected in the microscopic texture of the image. The ratio has been computed for each image of the panel at various empirical quantile levels t_α. In Figure 2, the distribution of the obtained ratios is summarized in a boxplot for each level.

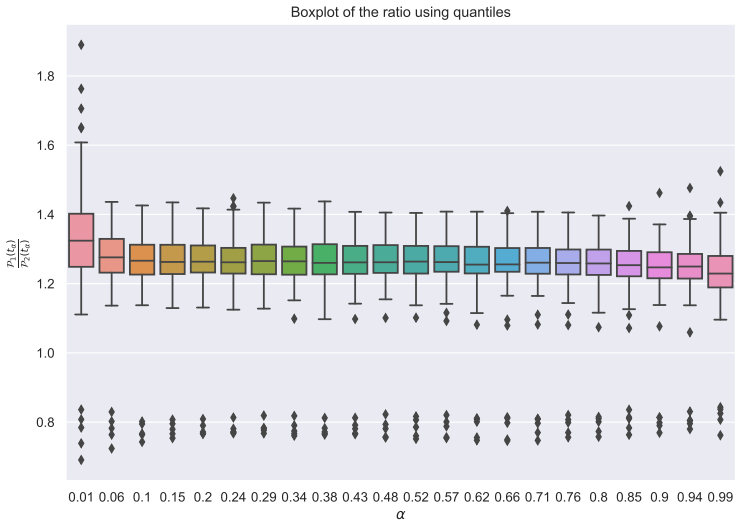

Figure 2: For $\alpha \in [0.01, 0.99]$, we represent the boxplot of the ratio between the two oriented perimeters computed at t_α level, $\mathcal{P}^1(t_\alpha), \mathcal{P}^2(t_\alpha)$, for stationary thresholded images of bone X-rays.

We observe that the boxplots of the ratio between the horizontal and vertical perimeters are not distributed around one, whatever the considered level. Moreover, for almost all images the observed ratios are above one whereas for some images extreme values are observed below one. We checked the fact that these below one extreme cases all belong to the same small group of images. Nevertheless, what is relevant on this sample of X-ray images of calcaneus is that the anisotropy of the texture can be revealed at any threshold level by simply comparing two single counters. It is worth to note that this anisotropy, although obvious through the proposed image analysis procedure, is not perceptible to the naked eye. With a very different approach based on quadratic variations, the same sample of images has been analyzed in Biermé et al. [2009] and the same conclusion has been obtained: the

calcaneus X-ray images are anisotropic.

Let us now present in details what is the content of our study. As already said, we aim at constructing a statistical test of isotropy based on the observation at small scale of the image. Our observation will be very sparse since it is reduced to count the horizontal and vertical edges that are involved at the interface between the black and the white pixels of the binary image. This geometrical quantity is nothing but the discrete perimeter (see Biermé and Desolneux [2021]), considering separately the horizontal contribution and the vertical one. In our inference only elementary steps are performed in order to compute this geometrical feature. This has a low computational cost compared for instance to isotropy-testing procedure based on spectral methods requiring matrix inversions (see e.g., Guan et al. [2004]).

Assuming that the original grey-level image is a discrete Gaussian stationary field, we are able to explicitly compute the first two moments of the so-called oriented perimeter. Our study of moments includes the asymptotic behavior as the number of pixels goes to infinity. We then establish a Central Limit Theorem for the joint oriented perimeters at various levels under a summability condition of the covariance function. The perimeter being given as a sum of functionals of correlated Gaussian variables, the main argument for the CLT that we use is borrowed from Breuer-Major result as exposed in Arcones [1994]. Let us note that a similar study was performed in Abaach et al. [2021] but under a very different context since the underlying Gaussian field was supposed to be a white noise. The induced totally independent structure of the pixels led to simple computations and estimations which are not allowed anymore in the correlated situation that we consider in the present paper.

The next step of our method consists in building the promised statistical test. More precisely, ρ being the covariance function of the Gaussian field and (e_1, e_2) being the canonical basis of $\mathbb{R}^2$, we consider the null hypothesis $H0 : \ \rho(e_1) = \rho(e_2)$ that we call "local isotropy" through a misuse of language. We exhibit a statistic depending on the ratio of the oriented perimeters that goes to one under $H0$ thanks to the CLT previously established. Moreover, we prove the consistency of the proposed test. Let us insist on the fact that our test is a non-parametric one so that the alternative hypothesis reduces to $H1 : \ \rho(e_1) \neq \rho(e_2)$. A by-product of our method is the measurement of the anisotropy through the ratio between

the oriented perimeters.

The theoretical study is completed by extensive numerical illustrations based on simulated data. We sample Gaussian fields with compact support covariances and use affine deformations to get anisotropic models. The performances of our test are illustrated on those models. The crucial question of estimating the variance of the perimeter is also explored. Finally, we apply our method to the calcaneus X-ray images that we have already presented. It allows us to infer properties and to estimate quantities that could be of interest from a medical point of view.

The paper is organized as follows. Section 2 is devoted to the presentation of the mathematical framework, namely the grid that defines the pixels and implies the discrete nature of the Gaussian random field that we use as a model for the grey-level image. We also precisely define the notion of discrete oriented perimeters that we consider all over the article. In Section 3, we proceed to the statistical study of the oriented perimeters by computing their first two moments and establishing a joint central limit theorem for both directions and various levels. Section 4 contains the numerical studies. This section is dedicated to Monte-Carlo estimations of the variance of the oriented perimeter for a Gaussian affine model and to numerical illustrations of the local isotropy test for the same toy model. The statistical analysis for bone X-rays images can be found Section 5. We end the paper by a concluding Section 6. Furthermore in the separated supplementary materials, Appendix A is devoted to a lemma that is used in the computation of the second moment (see Lemma A.1). In Appendix B we study an upper bound for the covariance of the oriented perimeter. In Appendix C we compute the covariance for the three cells configuration and finally some supplementary numerical studies can be found in Appendix D. Finally, in Appendix E we propose a comparison in terms of obtained p_{values} with the semivariogram based isotropy test proposed by Guan et al. [2004].

2 Mathematical framework

2.1 Construction of the binary image

Square tiling. Let m be an integer with $m \geq 2$. Without loss of generality, we consider our observation window as the unit square $S = [0, m]^2$ and we divide it into m^2 pairwise disjoint squares. We denote by e_1, e_2 the elements of the canonical basis of $\mathbb{R}^2$ and we

introduce the following notations.

- $\mathbb{G}_m := \big[0, m\big)^2 \cap \mathbb{Z}^2$ is the set of points in S that are considered. We write $x = (x_1, x_2)$ with $x_1, x_2 \in \{0, \dots, m-1\}$ for any $x \in \mathbb{G}_m$.
- For $x \in \mathbb{G}_m$, $C_m(x) := x + \big[0,1\big]^2$ will be referred to as a *cell*. Note that $S = \cup_{x \in \mathbb{G}_m} C_m(x)$.
- We denote by $\mathcal{E}_m^{(1)}$, $\mathcal{E}_m^{(2)}$ the set of vertical and horizontal edges in $\mathring{S}$, and for each $x \in \mathbb{G}_m$, we denote by $w_i(x)$ the intersection $C_m(x) \cap C_m(x + e_i)$ with $i \in \{1, 2\}$, that is an edge corresponding to a segment of length 1. And finally,

$$\mathbb{G}_m^{(1)} := \Big\{ x \in \mathbb{G}_m;\ C_m(x) \cap C_m(x + e_1) \subset \mathring{S} \Big\} = [\![0, m-2]\!] \times [\![0, m-1]\!],$$

$$\mathbb{G}_m^{(2)} := \Big\{ x \in \mathbb{G}_m;\ C_m(x) \cap C_m(x + e_2) \subset \mathring{S} \Big\} = [\![0, m-1]\!] \times [\![0, m-2]\!].$$

Figure 3 shows an example of a square tiling with $m = 4$.

Figure 3: Square tiling for $m = 4$ and associated cells $C_4((0,0))$ and $C_4((2,1))$ (green stripes). We represent the vertical edges w_1 in red and the horizontal ones w_2 in blue.

Square tiling and binary image. Using the previous square tiling, we observe $(X_x)_{x \in \mathbb{G}_m}$, which we assume coincides with values of a stationary random field $(X_x)_{x \in \mathbb{Z}^2}$. The stationarity hypothesis means that for all $h \in \mathbb{Z}^2$,

$$\big(X_{x+h}; x \in \mathbb{Z}^2\big) \overset{fdd}{=} \big(X_x; x \in \mathbb{Z}^2\big),$$

where fdd denotes finite-dimensional distributions. We denote by $\rho(x) := \mathrm{Cov}\,(X_0, X_x)$, $x \in \mathbb{Z}^2$, the covariance function of X. Considering a threshold parameter $t \in \mathbb{R}$, we introduce the associated binary image $Z_t^{(m)} = \big(\mathbb{1}_{\{X_x \geq t\}}\big)_{x \in \mathbb{G}_m}$ where each cell $C_m(x)$ is associated to black or white according to whether $X_x \geq t$ or $X_x < t$. In Figure 4 we display several random generations of Gaussian random fields and their associated thresholded images. Sampling is provided by using the Matlab function `stationary Gaussian process` MATLAB [2021]).

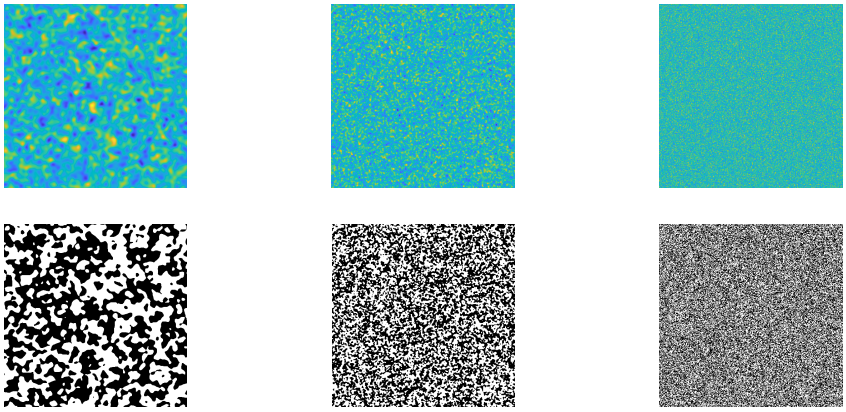

Figure 4: Generations of Gaussian random fields with covariance $\rho(x) = e^{-\kappa||x||^2}$ (first row) and their respective thresholded image $Z_t^{(m)}$ for $t = 0$ and $m = 512$ (second row). We consider various values for κ, from left to right $\kappa = 0.01, 0.1, 1$.

2.2 Oriented perimeter of a binary image

For $t \in \mathbb{R}$, let $Z^{(m)} = Z_t^{(m)}$ be the binary image at the given threshold $t \in \mathbb{R}$. Following the approach presented in Biermé and Desolneux [2021], for each edge $w \in \mathcal{E}_m = \mathcal{E}_m^{(1)} \cup \mathcal{E}_m^{(2)}$, we aim to know whether w contributes to the perimeter of the black component of $Z^{(m)}$ (see Figure 5). Making use of the additive nature of the perimeter, one can start by computing the oriented perimeter given each direction, horizontal and vertical .

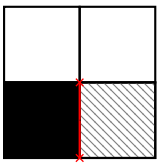

Figure 5: The edge $w_1((0,0))$ in red belongs to $C_2((0,0)) \cap C_2((1,0))$, with the cell $C_2((0,0))$ colored in black and $C_2((1,0))$ in gray dashed stripes.

Following this consideration, one can define the random quantity,

$$f_t^{(i)}(x) := \mathbb{1}_{\{\min(X_x, X_{x+e_i}) < t \leq \max(X_x, X_{x+e_i})\}}, \quad x \in \mathbb{G}_m^{(i)}, \tag{1}$$

in order to take into account the eventual contribution of the edge $w_i(x)$ to the perimeter of the black component of $Z^{(m)}$.

Let us now introduce the main tool of the present work.

Definition 2.1 (Oriented perimeter of a binary image $Z^{(m)}$)**.**
For $t \in \mathbb{R}$, we denote by $\mathcal{P}_m^{(i)}(t)$ the sum of all contributions over the ith direction (vertical for $i = 1$ and horizontal for $i = 2$) and we call it the oriented perimeter of the binary image $Z^{(m)}$,

$$\mathcal{P}_m^{(i)}(t) = \sum_{x \in \mathbb{G}_m^{(i)}} f_t^{(i)}(x). \tag{2}$$

The perimeter of $Z^{(m)}$ is given by $\mathcal{P}_m(t) := \mathcal{P}_m^{(1)}(t) + \mathcal{P}_m^{(2)}(t)$.

3 Statistics of the oriented perimeter

3.1 First moment

Let us start this study by investigating the first moment of the oriented perimeter $\mathcal{P}_m^{(i)}(t)$. The study of the second moment is postponed to Section 3.3.

Proposition 3.1 (First moment of the oriented perimeter)**.** *We assume that $(X_x)_{x \in \mathbb{G}_m}$ is a stationary Gaussian centered with unit variance random field. Let $i \in \{1, 2\}$ and let us denote by $\rho(e_i) = \mathrm{Cov}\,(X_0, X_{e_i}) \in [-1, 1]$. Let $t \in \mathbb{R}$, the expected value of the oriented perimeter in (2) is given by*

$$\mathbb{E}\left(\mathcal{P}_m^{(i)}(t)\right) = m(m-1)\mathbb{E}\left(f_t^{(i)}(0)\right) = m(m-1)h(t, \rho(e_i))$$

where

- *if $c \neq -1$,*

$$h(t, c) = \mathbb{E}\left(\Phi\left(\frac{2t + \sqrt{2(1-c)}|N|}{\sqrt{2(1+c)}}\right) - \Phi\left(\frac{2t - \sqrt{2(1-c)}|N|}{\sqrt{2(1+c)}}\right)\right) \tag{3}$$

  with $N \sim \mathcal{N}(0, 1)$ and Φ being the cumulative distribution function of the standard Gaussian,

- *if $c = -1$, $h(t, -1) = 2\left(1 - \Phi\left(|t|\right)\right)$.*

Proof. Considering the formula (2) for $\mathcal{P}_m^{(i)}(t)$ and applying the stationarity hypothesis, one can write that,

$$\mathbb{E}\left(\mathcal{P}_m^{(i)}(t)\right) = m(m-1)\mathbb{E}\left(f_t^{(i)}(0)\right),$$

with $\mathbb{E}\left(f_t^{(i)}(0)\right) = \mathbb{P}\left(\min\left(X_0, X_{e_i}\right) < t \leq \max\left(X_0, X_{e_i}\right)\right)$. We start by applying the following transformation to the Gaussian vector (X_0, X_{e_i}),

$$\Delta_0^{(i)} := X_{e_i} - X_0, \quad S_0^{(i)} := X_{e_i} + X_0.$$

The covariance matrix of the new Gaussian vector $(\Delta_0^{(i)}, S_0^{(i)})$ is given by $\widetilde{\Sigma}_i(0) = M\Sigma_i(0)M^\star$ with $M = \begin{pmatrix} -1 & 1 \\ 1 & 1 \end{pmatrix}$ and $\Sigma_i(0) = \begin{pmatrix} 1 & \rho(e_i) \\ \rho(e_i) & 1 \end{pmatrix}$. Thus, $\widetilde{\Sigma}_i(0) = \begin{pmatrix} 2(1-\rho(e_i)) & 0 \\ 0 & 2(1+\rho(e_i)) \end{pmatrix}$, which directly implies that the two variables $\Delta_0^{(i)}$ and $S_0^{(i)}$ are independent. Hence, we can write $\begin{cases} \Delta_0^{(i)} &= \sqrt{2(1-\rho(e_i))}U, \\ S_0^{(i)} &= \sqrt{2(1+\rho(e_i)}V, \end{cases}$ with $(U, V) \sim \mathcal{N}(0, I_2)$.
Let us now make an observation that will appear very useful in the following.

Remark 1. Let $a, b, t \in \mathbb{R}$, then

$$\min(a,b) \leq t \leq \max(a,b) \iff |2t - (a+b))| \leq |b-a|$$

The proof of this remark can be summarized in the following scheme. Let $a, b, t \in \mathbb{R}$,

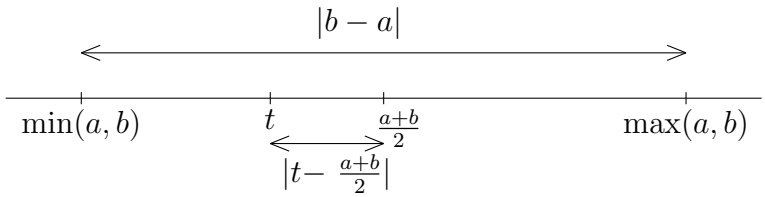

If $\rho(e_i) \neq -1$, by applying Remark 1 above we get

$$\begin{aligned}\mathbb{E}\left(f_t^{(i)}(0)\right) &= \mathbb{E}\left(\mathbb{1}_{\left\{\left|2t-S_0^{(i)}\right| \leq \left|\Delta_0^{(i)}\right|\right\}}\right) = \mathbb{E}\left(\mathbb{1}_{\left\{\frac{2t-\sqrt{2(1-\rho(e_i))}|U|}{\sqrt{2(1+\rho(e_i))}} \leq V \leq \frac{2t+\sqrt{2(1-\rho(e_i))}|U|}{\sqrt{2(1+\rho(e_i))}}\right\}}\right) \\ &= \mathbb{E}\left(\Phi\left(\frac{2t+\sqrt{2(1-\rho(e_i))}|U|}{\sqrt{2(1+\rho(e_i))}}\right) - \Phi\left(\frac{2t-\sqrt{2(1-\rho(e_i))}|U|}{\sqrt{2(1+\rho(e_i))}}\right)\right).\end{aligned}$$

If $\rho(e_i) = -1$, then there exists $N \sim \mathcal{N}(0,1)$ such that $(X_0, X_{e_i}) \overset{d}{=} (N, -N)$ and thus,

$$\mathbb{E}\left(f_t^{(i)}(0)\right) = \mathbb{P}\left(\min\left(N,-N\right) < t \leq \max\left(N,-N\right)\right) = \mathbb{P}\left(|t| \leq |N|\right) = 2\left(1 - \Phi\left(|t|\right)\right).$$

□

Proposition 3.1 extends the one given in Biermé and Desolneux [2021] (Proposition 3) where the expected perimeter is computed in the case $\rho(e_i) > 0$. We are also able to obtain an analytic expression for the first moment as stated in the next proposition.

Proposition 3.2 (Analytic expression for the first moment of the oriented perimeter)**.** *According to the notations in Proposition 3.1, for all* $t \in \mathbb{R}$ *and* $c \in (-1, 1]$

$$h(t,c) = \int_c^1 \frac{\exp(-t^2/(1+u))}{\pi\sqrt{(1-u^2)}} du. \tag{4}$$

Proof. Let $t \in \mathbb{R}$. We consider the function $h_t := h(t, \cdot)$ defined on $(-1, 1]$ through (3) and note that $h_t(1) = 0$.

We introduce an intermediate function $p_t(c) = \mathbb{E}\left(\Phi\left(\frac{2t + \sqrt{2(1-c)}|N|}{\sqrt{2(1+c)}}\right)\right)$. Using the symmetry properties of the cumulative distribution function Φ, we have $h_t(c) = p_t(c) - 1 + p_{-t}(c)$, thus h_t is smooth on $(-1, 1)$ and its derivative is equal to $h_t'(c) = p_t'(c) + p_{-t}'(c)$. Moreover, for all $c \in (-1, 1)$,

$$\begin{aligned}
p_t'(c) &= \mathbb{E}\left(\frac{-2|N| - t\sqrt{2(1-c)}}{2(1+c)\sqrt{1-c^2}}\Phi'\left(\frac{2t + |N|\sqrt{2(1-c)}}{\sqrt{2(1+c)}}\right)\right) \\
&= \frac{\exp(-t^2/(1+c))}{2\sqrt{2\pi}(1+c)\sqrt{1-c^2}} \\
&\quad \mathbb{E}\left(\left(-2|N| - t\sqrt{2(1-c)}\right)\exp\left(\frac{-t|N|\sqrt{2(1-c)}}{1+c}\right)\exp\left(\frac{-N^2(1-c)}{2(1+c)}\right)\right) \\
&= \frac{\exp(-t^2/(1+c))}{4\pi(1+c)\sqrt{1-c^2}} \\
&\quad \int_{-\infty}^{\infty} \exp\left(-\frac{y^2}{1+c}\right)\left(\left(-2|y| - t\sqrt{2(1-c)}\right)\exp\left(\frac{-t|y|\sqrt{2(1-c)}}{1+c}\right)\right) dy \\
&= \frac{\exp(-t^2/(1+c))}{2\pi(1+x)\sqrt{1-c^2}}\exp\left(\frac{t^2(1-c)}{2(1+c)}\right) \\
&\quad \int_0^{\infty}\left(-2y - t\sqrt{2(1-c)}\right)\exp\left(-\frac{\left(y + t\sqrt{2(1-c)}/2\right)^2}{1+c}\right) dy = \frac{-\exp(-t^2/(1+c))}{2\pi\sqrt{(1-c^2)}},
\end{aligned}$$

which gives us the result. □

Remark 2 (Degenerate dependence cases)**.**

- In the case of a fully dependent field, *i.e* $\rho(e_i) = 1$, then $\mathbb{E}\left(\mathcal{P}_m^{(i)}(t)\right) = 0$.
- In the case of a highly dependent field, *i.e* $\rho(e_i) \sim 1$, from Equation (4) we note that $h(t, \rho(e_i)) \sim \frac{\sqrt{1-\rho(e_i)}}{\pi\sqrt{2}}\exp(-t^2/2)$, as it has been stated in Biermé and Desolneux [2021] for a positively correlated field. In that case, the ratio $\mathbb{E}\left(\mathcal{P}_m^{(1)}(t)\right)/\mathbb{E}\left(\mathcal{P}_m^{(2)}(t)\right)$ is therefore invariant in regard to $t \in \mathbb{R}$.

- In the independent case, *i.e.* $\rho(e_i) = \mathrm{Cov}\,(X_0, X_{e_i}) = 0$, from (3) we can write,

$$\mathbb{E}\left(\mathcal{P}_m^{(i)}(t)\right) = m(m-1)\mathbb{E}\left(\Phi\left(\sqrt{2}t + |N|\right) - \Phi\left(\sqrt{2}t - |N|\right)\right) = 2m(m-1)\Phi(t)\left(1-\Phi(t)\right),$$

where we get the second identity by applying the variable change $(y,z) \mapsto (\frac{y-z}{\sqrt{2}}, \frac{y+z}{\sqrt{2}})$. In this *i.i.d.* setting, we recover the same result as in Abaach et al. [2021] (Proposition 3.1).

- At last, let us note that as in Abaach et al. [2021], in order to converge towards a non degenerate quantity when m goes to infinity, we have to consider a normalized perimeter thus, dividing the perimeter by the area of the window S, *i.e.* $\frac{1}{m^2}\mathcal{P}_m(t)$.

Total variation. In image processing, the total variation of an image $u \in L^1_{loc}(\mathbb{R}^2)$ which is given by $\int_S |\nabla u| dx$ is a common and well studied object. It is possible to link this quantity to the perimeter of u, by applying the coarea formula, $\int_S |\nabla u| dx = \int_{\mathbb{R}} \mathcal{P}(t) dt$ with $\mathcal{P}(t)$ being the perimeter associated to the level set of the image u at level t. In the following result, by considering Proposition (3.1), we obtain a simple expression for the first moment of the total variation and link it directly to $\rho(e_i)$, the covariance evaluated in the ith direction. It could be used as an estimator for $\rho(e_i)$.

Proposition 3.3. *Under the assumptions in Proposition 3.1, we get*

$$\int_{\mathbb{R}} \mathbb{E}\left(\mathcal{P}_m^{(i)}(t)\right) dt = \frac{2m(m-1)}{\sqrt{\pi}}\left(\sqrt{1-\rho(e_i)}\right). \tag{5}$$

Proof. Using Equation (3) in Proposition 3.1, we get,

$$\int_{\mathbb{R}} \mathbb{E}\left(\mathcal{P}_m^{(i)}(t)\right) dt$$

$$= \frac{m(m-1)}{2\pi}\int_{\mathbb{R}}\int_{\mathbb{R}}\int_{\mathbb{R}} e^{-\frac{1}{2}u^2} e^{-\frac{1}{2}v^2} \mathbb{1}_{\left\{\frac{\sqrt{2}t - \sqrt{1-\rho(e_i)}|u|}{\sqrt{1+\rho(e_i)}} \leq v \leq \frac{\sqrt{2}t + \sqrt{1-\rho(e_i)}|u|}{\sqrt{1+\rho(e_i)}}\right\}} du\, dv\, dt,$$

and using Fubini-Tonelli Theorem,

$$= \frac{m(m-1)}{2\pi}\int_{\mathbb{R}}\int_{\mathbb{R}} e^{-\frac{1}{2}u^2} e^{-\frac{1}{2}v^2}\left(\frac{2|u|\sqrt{1-\rho(e_i)}}{\sqrt{2}}\right) du\, dv = \frac{2}{\sqrt{\pi}} m(m-1)\sqrt{1-\rho(e_i)},$$

since $\mathbb{E}(|U|) = \sqrt{\frac{2}{\pi}}$. □

Let us now remark that in view of Proposition 3.2, for all $t \in \mathbb{R}$, we have $c \mapsto h(t,c)$ strictly non-increasing on $(-1,1)$. It follows that the corresponding result holds for the oriented perimeter.

Proposition 3.4. *Let $\overline{X}, \widetilde{X}$ be two stationary centered Gaussian random fields with unit variance, and $\bar{\rho}, \widetilde{\rho}$ their respective covariance structure. We have the following result: for $1 \leq i, j \leq 2$,*

$$\text{if} \quad \widetilde{\rho}(e_i) < \bar{\rho}(e_j) \quad \text{then} \quad \mathbb{E}\left(\mathcal{P}^{(i)}_{m,\widetilde{\rho}}(t)\right) > \mathbb{E}\left(\mathcal{P}^{(j)}_{m,\bar{\rho}}(t)\right), \ \forall t \in \mathbb{R}.$$

As a consequence, $\mathbb{E}\left(\mathcal{P}^{(1)}_m(t)\right) \neq \mathbb{E}\left(\mathcal{P}^{(2)}_m(t)\right)$ if and only if $\rho(e_1) \neq \rho(e_2)$. Now, assuming that the field X is isotropic, one consequence would be that $\rho(e_1) = \rho(e_2)$ which is equivalent to $\frac{\mathbb{E}\left(\mathcal{P}^{(1)}_m(t)\right)}{\mathbb{E}\left(\mathcal{P}^{(2)}_m(t)\right)} = 1$. Then, the ratio $\mathcal{P}^{(1)}_m(t)/\mathcal{P}^{(2)}_m(t)$ would be distributed around 1 in the case of isotropy. This consideration, that will be crucial for the proposed local isotropy testing procedure, is discussed in the next section.

3.2 Local isotropy test using the oriented perimeters

In order to construct a local isotropy test using the oriented perimeters of the binary image, we first establish a Central Limit Theorem for the variables $(\mathcal{P}^{(i)}_m(t))_m$. To do that, we add some assumptions on the covariance function ρ of the field X.

($\mathcal{A}1$) $\lim_{m\to\infty} m^{-2} \sum_{x,y\in\mathbb{G}_m} \rho(x-y+h)$ exists for all $h \in \{0, e_i, e_j, e_i - e_j; 1 \leq i, j \leq 2\}$.

($\mathcal{A}2$) $\lim_{m\to\infty} m^{-1} \sum_{k,l=0}^{m} \rho((k-l)e_i + \varepsilon e_j)$ exists for all $\{i, j\} = \{1, 2\}$ and $\varepsilon \in \{0, 1\}$.

($\mathcal{A}3$) $\lim_{m\to\infty} m^{-2} \sum_{x,y\in\mathbb{G}_m} \rho(x - \ y)^2$ exists.

Note that if $\sum |\rho(x)| < \infty$ then it also fulfills the three Assumptions ($\mathcal{A}1$), ($\mathcal{A}2$) and ($\mathcal{A}3$).

Theorem 3.5. *(Multi-directional multivariate CLT for r-thresholds). We consider that $(X_x)_{x\in\mathbb{Z}^2}$ is a stationary standard Gaussian field with a covariance function that satisfies ($\mathcal{A}1$), ($\mathcal{A}2$) and ($\mathcal{A}3$). Let r be a positive integer and $t_1, \cdots, t_r \in \mathbb{R}$. Then,*

$$\frac{1}{m}\left(\begin{pmatrix} \mathcal{P}^{(1)}_m(t_1) \\ \vdots \\ \mathcal{P}^{(1)}_m(t_r) \\ \mathcal{P}^{(2)}_m(t_2) \\ \vdots \\ \mathcal{P}^{(2)}_m(t_r) \end{pmatrix} - \begin{pmatrix} \mathbb{E}(\mathcal{P}^{(1)}_m(t_1)) \\ \vdots \\ \mathbb{E}(\mathcal{P}^{(1)}_m(t_r)) \\ \mathbb{E}(\mathcal{P}^{(2)}_m(t_1)) \\ \vdots \\ \mathbb{E}(\mathcal{P}^{(2)}_m(t_r)) \end{pmatrix}\right) \xrightarrow[m\to\infty]{d} \mathcal{N}\left(0, \Sigma^{\star}_{2r}\right),$$

where $\xrightarrow{d}$ *stands for the convergence in distribution and* $\mathcal{N}\left(0,\, \Sigma^{\star}_{2r}\right)$ *for the* $2r$*-dimensional centered Gaussian distribution with covariance matrix* $\Sigma^{\star}_{2r}$ *given by*

$$\Sigma^{\star}_{2r}(l,i,k,j) := \lim_{m\to\infty} \mathrm{Cov}\left(\frac{1}{m}\mathcal{P}^{(i)}_m(t_l), \frac{1}{m}\mathcal{P}^{(j)}_m(t_k)\right) \text{ for } i,j \in \{1,2\} \text{ and } k,l \in \{1,\dots,r\}. \quad (6)$$

Proof. For the sake of simplicity, we will prove the theorem for one threshold (*i.e.* $r=1$), the generalized case can be established by following a similar procedure.

Let $t \in \mathbb{R}$. Using the Cramèr-Wold method, we will prove that for each $(a_1,a_2) \in \mathbb{R}^2$, we have

$$\frac{a_1}{m}\left(\mathcal{P}^{(1)}_m(t) - \mathbb{E}\left(\mathcal{P}^{(1)}_m(t)\right)\right) + \frac{a_2}{m}\left(\mathcal{P}^{(2)}_m(t) - \mathbb{E}\left(\mathcal{P}^{(2)}_m(t)\right)\right) \xrightarrow[m\to\infty]{d} \mathcal{N}\left(0,\, \sigma^2(t)\right)$$

with $\sigma^2(t) < \infty$. For $x \in \mathbb{G}_m$, by using the notation introduced in (1), we consider the 3-dimensional Gaussian vector $\mathbb{X}_x = (\mathbb{X}^{(i)}_x)_{1\le i\le 3} = (X_x, X_{x+e_1}, X_{x+e_2})$ and the function g_t defined on $\mathbb{R}^3$,

$$g_t(u,v,w) := a_1 \mathbb{1}_{\{\min(u,v)<t\le\max(u,v)\}} + a_2 \mathbb{1}_{\{\min(u,w)<t\le\max(u,w)\}}.$$

Hence, re-writing the following sum, we get

$$\sum_{x\in\mathbb{G}_m} g_t(\mathbb{X}_x) = \sum_{x_1=0}^{m-1}\sum_{x_2=0}^{m-1} g_t(\mathbb{X}_{x_1,x_2}) = a_1\mathcal{P}^{(1)}_m(t) + a_2\mathcal{P}^{(2)}_m(t) + A^{(1)}_m + A^{(2)}_m,$$

where

$$A^{(1)}_m = a_1 \sum_{x_2=0}^{m-1} f^{(1)}_t(m-1,x_2) \text{ and } A^{(2)}_m = a_2 \sum_{x_1=0}^{m-1} f^{(2)}_t(x_1,m-1).$$

Note that $|g(t)| \le |a_1| + |a_2|$, thus, $\mathbb{E}\left(g_t(\mathbb{X}_{0,0})^2\right) < (|a_1|+|a_2|)^2$. On the one hand, under $(\mathcal{A}1)$, for all $1 \le p,q \le 3$,

$$\lim_{m\to\infty} m^{-2} \sum_{x\in\mathbb{G}_m}\sum_{y\in\mathbb{G}_m} \mathbb{E}\left(\mathbb{X}^{(p)}_x \mathbb{X}^{(q)}_y\right) \quad \text{exists},$$

since ρ is the covariance function of X. On the other hand, $(\mathcal{A}3)$ implies that $\sum_{x\in\mathbb{Z}^2}\rho(x)^2 < +\infty$. Indeed, it comes from Fatou's Lemma using the fact that

$$\frac{1}{m^2}\sum_{x,y\in\mathbb{G}_m}\rho(x-y)^2 = \sum_{|x_1|<m}\sum_{|x_2|<m}\left(1-\frac{|x_1|}{m}\right)\left(1-\frac{|x_2|}{m}\right)\rho(x)^2.$$

Applying again Fatou's lemma yields the existence of

$$\lim_{m\to\infty} m^{-2} \sum_{x\in\mathbb{G}_m}\sum_{y\in\mathbb{G}_m} \mathbb{E}\left(\mathbb{X}^{(p)}_x \mathbb{X}^{(q)}_y\right)^2 \ \forall p,q \in \{1,2,3\}.$$

Hence, we can apply Theorem 2 in Arcones [1994] and get that

$$m^{-1} \sum_{x \in \mathbb{G}_m^{(1)}} g_t\left(\mathbb{X}_x\right) - \mathbb{E}\left(g_t\left(\mathbb{X}_x\right)\right) \xrightarrow[m\to\infty]{d} \mathcal{N}\left(0,\, \sigma^2(t)\right).$$

Now, it only remains to check that $\frac{1}{m} A_m^{(i)}$ tends to 0 in probability for $1 \leq i \leq 2$. Let us verify it for $A_m^{(1)}$. By stationarity, the random variable $A_m^{(1)}$ has the same law as

$$\widetilde{A}_m^{(1)} = \sum_{x_2=0}^{m-1} \widetilde{g}_t(X_{0,x_2}, X_{1,x_2}), \quad \text{where } \widetilde{g}_t(u,v) = a_1 \mathbb{1}_{\{\min(u,v)<t\leq \max(u,v)\}}.$$

Then, Assumptions $(\mathcal{A}2)$ and $(\mathcal{A}3)$ ensure that we can again apply Theorem 2 in Arcones [1994] so that the convergence in distribution of $\left(\frac{1}{m^{1/2}}\left(\widetilde{A}_m^{(1)} - \mathbb{E}(\widetilde{A}_m^{(1)})\right)\right)_m$ implies that $\left(\frac{1}{m}\left(\widetilde{A}_m^{(1)} - \mathbb{E}(\widetilde{A}_m^{(1)})\right)\right)_m$ tends to 0 in probability.

□

We are now in position to construct the promised isotropy test. As previously discussed, we now aim to build a test using the specific structure of the mean perimeter in the case of local isotropy. Let us consider the null hypothesis

$$H_0 \;:\; \rho(e_1) = \rho(e_2).$$

Under H_0, let us remark that $\mathbb{E}\left(\mathcal{P}_m^{(1)}(t)\right) = \mathbb{E}\left(\mathcal{P}_m^{(2)}(t)\right)$ and $\mathbb{V}\left(\mathcal{P}_m^{(1)}(t)\right) = \mathbb{V}\left(\mathcal{P}_m^{(2)}(t)\right)$ for all t. Making use of Theorem 3.5, we have the following Gaussian asymptotic result.

Proposition 3.6 (CLT for the ratio of oriented perimeters)**.** *Let $t \in \mathbb{R}$ and $\mathcal{P}_m^{(i)}(t)$ be the oriented perimeter over ith-direction ($i = 1, 2$) introduced in Definition 2.1. Under the same assumptions as in Theorem 3.5, it holds that,*

$$\frac{1}{m}\left(\frac{\mathcal{P}_m^{(1)}(t)}{\mathcal{P}_m^{(2)}(t)} - \frac{\mathbb{E}\left(\mathcal{P}_m^{(1)}(t)\right)}{\mathbb{E}\left(\mathcal{P}_m^{(2)}(t)\right)}\right) \xrightarrow[m\to\infty]{d} \mathcal{N}\left(0, \widetilde{\sigma}^2(t)\right), \tag{7}$$

with $\widetilde{\sigma}^2(t) = \frac{\widetilde{\sigma}_{1,1}(t)\mu_2(t)^2 - 2\mu_2(t)\mu_1(t)\widetilde{\sigma}_{1,2}(t) + \widetilde{\sigma}_{2,2}(t)\mu_1(t)^2}{\mu_2(t)^4}$, $\mu_i(t) = h(t, \rho(e_i))$ *as in* (3) *and* $\widetilde{\sigma}_{i,j}(t) = \Sigma_2^\star(1, i, 1, j)$ *as in* (6).

Furthermore, under H_0, it holds that

$$\frac{1}{m}\left(\frac{\mathcal{P}_m^{(1)}(t)}{\mathcal{P}_m^{(2)}(t)} - 1\right) \xrightarrow[m\to\infty]{d,H_0} \mathcal{N}\left(0, \widetilde{\sigma}_{H_0}^2(t)\right), \tag{8}$$

with $\widetilde{\sigma}_{H_0}^2(t) = \frac{2(\widetilde{\sigma}_{1,1}(t) - \widetilde{\sigma}_{1,2}(t))}{\mu_2(t)^2}$.

Proposed test with asymptotic level α. Let $t \in \mathbb{R}$ and let us introduce the following ratio,

$$R_m(t) = \frac{\mathcal{P}_m^{(1)}(t)}{\mathcal{P}_m^{(2)}(t)}.$$

Considering a consistent empirical estimator $\widehat{\sigma}_m^2(t)$ of $\widetilde{\sigma}^2(t)$, then, from Proposition 3.6, it holds that

$$\frac{1}{m\sqrt{\widehat{\sigma}_m^2(t)}}\left(R_m(t) - 1\right) \xrightarrow[m\to\infty]{d,H_0} \mathcal{N}(0,1).$$

Take a confidence level $\alpha \in (0,1)$ and set $q_{1-\frac{\alpha}{2}}$ such that $\mathbb{P}\left(|\mathcal{N}(0,1)| \leq q_{1-\frac{\alpha}{2}}\right) = 1 - \frac{\alpha}{2}$. We define the symmetric accessible test $\widehat{\phi}_m(t)$ with asymptotic level α as

$$\widehat{\phi}_m(t) = \mathbb{1}_{\left\{\frac{1}{m\sqrt{\widehat{\sigma}_m^2(t)}}|(R_m((t)-1)|\geq q_{1-\frac{\alpha}{2}}\right\}}. \tag{9}$$

Let us now raise the consistency question of the proposed test statistic under the alternative hypothesis $H_1 : \rho(e_1) \neq \rho(e_2)$. According to Proposition 3.4, if $\rho(e_1) \neq \rho(e_2)$ then $\mathbb{E}\left(\mathcal{P}_m^1(t)\right)/\mathbb{E}\left(\mathcal{P}_m^2(t)\right) \neq 1$, for all $t \in \mathbb{R}$. Hence, we have the following result.

Proposition 3.7 (Consistency of the proposed isotropy test)**.** *For all $t \in \mathbb{R}$,*

$$\mathbb{P}_{H_1}\left(\widehat{\phi}_m(t) = 1\right) \to 1, \quad \textit{for} \quad m \to \infty.$$

Theorem 3.5 insures the existence of the asymptotic covariance of the oriented perimeter but does not give any information regarding the expression of the covariance. In the following section, we aim to focus on the second moment of the perimeter.

3.3 Theoretical study of the covariance of the oriented perimeter

Let us consider a stationary Gaussian random field $(X_x)_{x\in\mathbb{Z}^2}$ with zero mean and unit variance whose covariance structure is given by $\rho(x) = \mathrm{Cov}(X_0, X_x)$. Let us assume that $|\rho(e_i)| < 1$ and that ρ corresponds to a spectral measure that has a density.

Lemma 3.8. *Let $s, t \in \mathbb{R}$,*

$$\mathrm{Cov}\left(\mathcal{P}_m(t), \mathcal{P}_m(s)\right) = \sum_{1\leq i,j\leq 2} \mathrm{Cov}(\mathcal{P}_m^{(i)}(t), \mathcal{P}_m^{(j)}(s)) \tag{10}$$

with

$$\mathrm{Cov}\left(\mathcal{P}_m^{(1)}(t),\mathcal{P}_m^{(1)}(s)\right)=\sum_{x_2=(1-m)}^{m-1}\sum_{x_1=(2-m)}^{m-2}\left(m-|x_2|\right)\left(m-1-|x_1|\right)\mathrm{Cov}\left(f_t^{(1)}(0),f_s^{(1)}(x)\right),$$

$$\mathrm{Cov}\left(\mathcal{P}_m^{(2)}(t),\mathcal{P}_m^{(2)}(s)\right)=\sum_{x_1=(1-m)}^{m-1}\sum_{x_2=(2-m)}^{m-2}\left(m-|x_1|\right)\left(m-1-|x_2|\right)\mathrm{Cov}\left(f_t^{(2)}(0),f_s^{(2)}(x)\right),$$

and finally,

$$\mathrm{Cov}\left(\mathcal{P}_m^{(1)}(t),\mathcal{P}_m^{(2)}(s)\right)=\sum_{x_1=2-m}^{m-1}\sum_{x_2=1-m}^{m-2}\left(m-|x_1|-\mathbb{1}_{x_1\le 0}\right)\left(m-|x_2|-\mathbb{1}_{x_2\ge 0}\right)\mathrm{Cov}\left(f_t^{(1)}(0),f_s^{(2)}(x)\right).$$

Proof. Let us start with the computation of $\mathrm{Cov}(\mathcal{P}_m^{(1)}(t),\mathcal{P}_m^{(1)}(s))$. By stationarity, we have

$$\mathrm{Cov}(\mathcal{P}_m^{(1)}(t),\mathcal{P}_m^{(1)}(s))=\sum_{x\in\mathbb{G}_m^{(1)}}\sum_{y\in\mathbb{G}_m^{(1)}}\mathrm{Cov}\left(f_t^{(1)}(0),f_s^{(1)}(y-x)\right).$$

For $z_1=y_1-x_1$ one has

$$\begin{cases}0\le x_1\le m-2\\ 0\le y_1\le m-2\end{cases}\Leftrightarrow\begin{cases}2-m\le z_1\le m-2\\ \max(0,-z_1)\le x_1\le\min(m-2,m-2-z_1)\end{cases},$$

and similarly for $z_2=y_2-x_2$

$$\begin{cases}0\le x_2\le m-1\\ 0\le y_2\le m-1\end{cases}\Leftrightarrow\begin{cases}1-m\le z_2\le m-1\\ \max(0,-z_2)\le x_2\le\min(m-1,m-1-z_2)\end{cases}.$$

Thus,

$$\mathrm{Cov}\left(\mathcal{P}_m^{(1)}(t),\mathcal{P}_m^{(1)}(s)\right)=\sum_{z_1=(2-m)}^{m-2}\sum_{z_2=(1-m)}^{m-1}\left(m-1-|z_1|\right)\left(m-|z_2|\right)\mathrm{Cov}\left(f_t^{(1)}(0),f_s^{(1)}(z)\right).$$

For $\mathrm{Cov}\left(\mathcal{P}_m^{(1)}(t),\mathcal{P}_m^{(2)}(s)\right)$, we still have by stationarity

$$\mathrm{Cov}\left(\mathcal{P}_m^{(1)}(t),\mathcal{P}_m^{(2)}(s)\right)=\sum_{x\in\mathbb{G}_m^{(1)}}\sum_{y\in\mathbb{G}_m^{(2)}}\mathrm{Cov}\left(f_t^{(1)}(0),f_s^{(2)}(y-x)\right),$$

and again, considering $z_1=y_1-x_1$ and $z_2=y_2-x_2$, we get

$$\begin{aligned}&\mathrm{Cov}\left(\mathcal{P}_m^{(1)}(t),\mathcal{P}_m^{(2)}(s)\right)\\&\quad=\sum_{z_1=2-m}^{m-1}\sum_{z_2=1-m}^{m-2}\left(m-|z_1|-\mathbb{1}_{z_1\le 0}\right)\left(m-|z_2|-\mathbb{1}_{z_2\ge 0}\right)\mathrm{Cov}\left(f_t^{(1)}(0),f_s^{(2)}(z)\right).\end{aligned}$$

□

Lemma 3.8 shows that getting the value of the covariance $\mathrm{Cov}\left(\mathcal{P}_m(t), \mathcal{P}_m(s)\right)$ requires the computation of all the elements $\mathrm{Cov}\left(f_t^{(i)}(0), f_s^{(j)}(x)\right)$, $i, j \in \{1, 2\}$. Any of such elements has a two, three or four cells structure, depending on the cardinality of the set $\{C_m(0), C_m(e_i), C_m(x), C_m(x + e_j)\}$. Figure 6 below shows the five types of configurations depending on the orientations i, j and the position of x on the grid.

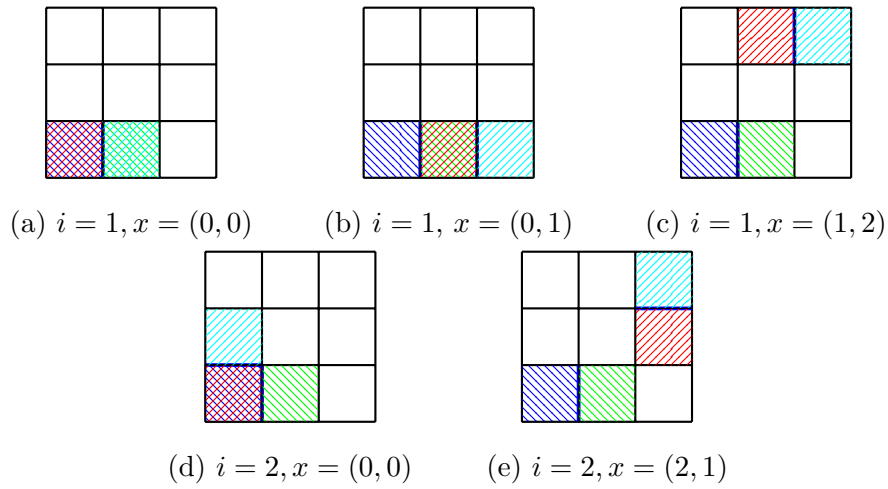

(a) $i = 1, x = (0, 0)$ (b) $i = 1$, $x = (0, 1)$ (c) $i = 1, x = (1, 2)$

(d) $i = 2, x = (0, 0)$ (e) $i = 2, x = (2, 1)$

Figure 6: Illustrations of the two, three and four cells configuration involved in the computation of $\mathrm{Cov}\left(f_t^{(1)}(0), f_s^{(i)}(x)\right)$ in Lemma 3.8.

Remark 3. The existence of the spectral density insures that the covariance matrix of any Gaussian vector of type $(X_{x_i})_{1 \le i \le n}$ is invertible as soon as the points $(x_i)_{1 \le i \le n}$ are distinct from one another (see Lemma A.1 in Appendix A). Thus, the computation of previous sums in Lemma 3.8 breaks down as 2-cells contribution (see configuration (a) in Figure 6), 3-cells (configurations (b) and (d)) and finally the 4-cells one (configurations (c) and (e)), where the involved Gaussian vector is non-degenerate whatever the configuration.

We first start with the 2-cells case (*see* Lemma 3.9 below), which corresponds to the computation of the term $\mathrm{Cov}\left(f_t^{(1)}(0), f_s^{(1)}(0)\right)$, the 4-cells case is computed in Proposition 3.10 and finally, the 3-cells case will be studied in Appendix C.

Lemma 3.9 (Computation of the two cells contribution)**.** *Let $Z \sim \mathcal{N}(0, 1)$. It holds that*

$$\mathbb{E}\left(f_t^{(1)}(0) f_s^{(1)}(0)\right) = \mathbb{E}\left(\left(\Phi\left(\frac{\sqrt{2}\max(t,s) + \sqrt{1-\rho(e_1)}|Z|}{\sqrt{1+\rho(e_1)}}\right) - \Phi\left(\frac{\sqrt{2}\min(t,s) - \sqrt{1-\rho(e_1)}|Z|}{\sqrt{1+\rho(e_1)}}\right)\right) \mathbb{1}_{\left\{(|s-t| \le |Z|\sqrt{2(1-\rho(e_1))}\right\}}\right).$$

Proof. We apply the same strategy we used in the proof of Proposition 3.1. □

Proposition 3.10 (Computation of the four cells contribution)**.** *Let $i = 1$ or 2, and let $x \in \mathbb{Z}^2$ such that the covariance matrix $\Sigma_i(x)$ of the Gaussian vector $(X_0, X_{e_1}, X_x, X_{x+e_i})$ is invertible. Let us define the following coefficients,*

$$\Delta\rho(x) = \rho(x - e_1) - \rho(x) \text{ and } S\rho(x) = \rho(x - e_1) + \rho(x).$$

Then, we are able to introduce the following quantities,

$$\begin{cases} \sigma_1^{(-)} &= \sqrt{2(1-\rho(e_1))} \\ \sigma_1^{(+)} &= \sqrt{2(1+\rho(e_1))} \end{cases}$$

$$\begin{cases} \pi_U^{(-,i)}(x) &= \frac{1}{\sigma_1^{(-)}}\left(\Delta\rho(x+e_i) - \Delta\rho(x)\right) \\ \pi_V^{(-,i)}(x) &= \frac{1}{\sigma_1^{(+)}}\left(S\rho(x+e_i) - S\rho(x)\right) \\ \pi_W^{(-,i)}(x) &= \left(2(1-\rho(e_i)) - \pi_U^{(-,i)}(x)^2 - \pi_V^{(-,i)}(x)^2\right)^{(1/2)} \end{cases}$$

$$\begin{cases} \pi_U^{(+,i)}(x) &= \frac{1}{\sigma_1^{(-)}}\left(\Delta\rho(x) + \Delta\rho(x+e_i)\right) \\ \pi_V^{(+,i)}(x) &= \frac{1}{\sigma_1^{(+)}}\left(S\rho(x) + S\rho(x+e_i)\right) \\ \pi_W^{(+,i)}(x) &= \frac{-1}{\pi_W^{(-,i)}(x)}\left(\pi_U^{(-,i)}(x)\pi_U^{(+,i)}(x) + \pi_V^{(-,i)}(x)\pi_V^{(+,i)}(x)\right) \\ \pi_Z^{(+,i)}(x) &= \left(2(1+\rho(e_i)) - \pi_U^{(+,i)}(x)^2 - \pi_V^{(+,i)}(x)^2 - \pi_W^{(+,i)}(x)^2\right)^{(1/2)}, \end{cases}$$

where $\sigma_1^{(-)} > 0$, $\sigma_1^{(+)} > 0$, $\pi_W^{(-,i)}(x) > 0$ and $\pi_Z^{(+,i)}(x) > 0$. Moreover,

$$\begin{aligned} &\mathbb{E}\left(f_t^{(1)}(0) f_s^{(i)}(x)\right) = \mathbb{E}\Bigg(\mathbb{1}_{\left\{|2t - \sigma_1^{(+)}V| \le \sigma_1^{(-)}|U|\right\}} \\ &\Big|\Phi_{\pi_Z^{(+,i)}(x)}\left(2s + \left(\pi_U^{(-,i)}(x) - \pi_U^{(+,i)}(x)\right)U + \left(\pi_V^{(-,i)}(x) - \pi_V^{(+,i)}(x)\right)V + \left(\pi_W^{(-,i)}(x) - \pi_W^{(+,i)}(x)\right)W\right) \\ &-\Phi_{\pi_Z^{(+,i)}(x)}\left(2s - \left(\pi_U^{(-,i)}(x) + \pi_U^{(+,i)}(x)\right)U - \left(\pi_V^{(-,i)}(x) + \pi_V^{(+,i)}(x)\right)V - \left(\pi_W^{(+,i)}(x) + \pi_W^{(-,i)}(x)\right)W\right)\Big|\Bigg) \end{aligned} \tag{11}$$

with $\Phi_{\pi_Z^{(+,i)}(x)}$ the $\mathcal{N}(0, (\pi_Z^{(+,i)}(x))^2)$-cumulative distribution function and $(U, V, W) \sim \mathcal{N}(0, I_3)$.

Proof. Let us define the following Gaussian variables

$$\Delta_x^{(i)} := X_{x+e_i} - X_x \text{ and } S_x^{(i)} := X_{x+e_i} + X_x. \tag{12}$$

The covariance matrix of the Gaussian vector $(\Delta_0^{(1)}, S_0^{(1)}, \Delta_x^{(i)}, S_x^{(i)})$ is equal to $\widetilde{\Sigma}_i(x) = \begin{pmatrix} A_1 & B_i(x) \\ B_i^\star(x) & A_i \end{pmatrix}$ with $A_i = \begin{pmatrix} 2(1-\rho(e_i)) & 0 \\ 0 & 2(1+\rho(e_i)) \end{pmatrix}$ and $B_i(x) = \begin{pmatrix} \Delta\rho(x+e_i) - \Delta\rho(x) & \Delta\rho(x) + \Delta\rho(x+e_i) \\ S\rho(x+e_i) - S\rho(x) & S\rho(x) + S\rho(x+e_i) \end{pmatrix}$. We assume that $\widetilde{\Sigma}_i(x)$ is invertible,

thus, applying the Cholesky decomposition yields the existence of an invertible lower triangular matrix $L(x)$ such that $\widetilde{\Sigma}_i(x) = L(x)L(x)^\star$. The matrix $L(x)$ is given by $L(x) = \begin{pmatrix} \sigma_1^{(-)} & 0 & 0 & 0 \\ 0 & \sigma_1^{(+)} & 0 & 0 \\ \pi_U^{(-,i)}(x) & \pi_V^{(-,i)}(x) & \pi_W^{(-,i)}(x) & 0 \\ \pi_U^{(+,i)}(x) & \pi_V^{(+,i)}(x) & \pi_W^{(+,i)}(x) & \pi_Z^{(+,i)}(x) \end{pmatrix}$ with the coefficients introduced in the statement of Proposition 3.10. Furthermore, $\det(L(x)) \neq 0$ implies that $\sigma_1^{(\pm)} \neq 0$, $\pi_W^{(-,i)}(x) \neq 0$ and $\pi_Z^{(+,i)}(x) \neq 0$ as stated in the quoted Proposition. This decomposition allows us to write $\begin{pmatrix} \Delta_0^{(1)} \\ S_0^{(1)} \\ \Delta_x^{(i)} \\ S_x^{(i)} \end{pmatrix} = L(x) \begin{pmatrix} U \\ V \\ W \\ Z \end{pmatrix}$, with $(U,V,W,Z) \sim \mathcal{N}(0, I_4)$. Developing the indicator functions, we get the following expression

$$\begin{aligned}
\mathbb{E}\left(f_t^{(1)}(0) f_s^{(i)}(x)\right) &= \mathbb{E}\left(\mathbb{1}_{\left\{|2t - S_0^{(1)}| \leq |\Delta_0^{(1)}|\right\}} \mathbb{1}_{\left\{|2s - S_x^{(i)}| \leq |\Delta_x^{(i)}|\right\}}\right) \\
&= \mathbb{E}\left(\mathbb{1}_{\left\{|2t - S_0^{(1)}| \leq |\Delta_0^{(1)}|\right\}} \mathbb{1}_{\left\{2s - \pi_U^{(+,i)}(x)U - \pi_V^{(+,i)}(x)V - \pi_W^{(+,i)}(x)W - |\Delta_x^{(i)}| \leq \pi_Z^{(+,i)}(x)Z \right.}\right. \\
&\qquad \left.\left. \leq 2s - \pi_U^{(+,i)}(x)U - \pi_V^{(+,i)}(x)V - \pi_W^{(+,i)}(x)W + |\Delta_x^{(i)}|\right\}\right).
\end{aligned}$$

The variable $\pi_Z^{(+,i)} Z \sim \mathcal{N}\left(0, \pi_Z^{(+,i)}(x)^2\right)$ and $\Phi_{\pi_Z^{(+,i)}(x)}$ being an increasing function, we get

$$\begin{aligned}
\mathbb{E}\left(f_t^{(1)}(0) f_s^{(i)}(x)\right) = \mathbb{E}\Bigg(&\mathbb{1}_{\left\{|2t - \sigma_1^{(+)}V| \leq \sigma_1^{(-)}|U|\right\}} \\
&\Big|\Phi_{\pi_Z^{(+,i)}(x)}\left(2s - \pi_U^{(+,i)}(x)U - \pi_V^{(+,i)}(x)V - \pi_W^{(+,i)}(x)W + \Delta_x^{(i)}\right) \\
&- \Phi_{\pi_Z^{(+,i)}(x)}\left(2s - \pi_U^{(+,i)}(x)U - \pi_V^{(+,i)}(x)V - \pi_W^{(+,i)}(x)W - \Delta_x^{(i)}\right)\Big|\Bigg),
\end{aligned}$$

which directly gives (11). □

In Appendix B we explore the link between $\mathrm{Cov}\left(f_t^{(1)}(0), f_s^{(i)}(x)\right)$ and the field covariance function ρ and exhibit an explicit upper bound for the covariance of the oriented perimeter.

Estimation methods of the variance. We are going to consider two approaches for estimating the variance $\widetilde{\sigma}^2(t)$ in Proposition 3.6, both relying on a classical empirical variance estimator. The first approach relies on having n independent realizations of the random field $(X_x)_{x \in \mathbb{G}_m}$ (*i.e* n-images of size m), we start by fixing the threshold level t and

computing the ratio $(R_{m,i}(t))_{i\leq n}$ for all n images. Then we consider the classical empirical estimator of the variance denoted here $\widehat{\sigma}^{(1)}_{n,m}(t)$. In the following we will refer to this method as *the Monte-Carlo* method. The second considered method is inspired by Di Bernardino and Duval [2020] and is referred to as the *sub-window* method. It consists in dividing the window S in $M_n \in \mathbb{N}$ patches, computing the ratio on each individual patch and computing the classical empirical variance estimator, denoted here $\widehat{\sigma}^{(2)}_{M_m,m}(t)$. To establish the consistency of the estimator, we compute it on domains that are infinitely distant, mimicking the classical context of *i.i.d.* random variables described above. Let us now proceed to numerical studies to illustrate the theoretical results.

4 Numerical studies

4.1 Numerical studies of moments of the oriented perimeter

The model we use to illustrate the test, is a parametric model that belongs to the class of affine Gaussian processes with a covariance function of compact support, commonly known as m-dependent field. The parameter m designates the range of dependence meaning that for $||x||_2 > m$, $\mathrm{Cov}\,(X_0, X_x) = 0$ and in particular $\mathrm{Cov}\left(f^{(1)}_t(0), f^{(i)}_s(x)\right) = 0$. This model falls within the framework of the Central Limit Theorem 3.5. The parametric nature proves to be advantageous in the analysis of the behavior of the test under the alternative hypothesis $(H1)$. Let X be a stationary, isotropic centered Gaussian field with a spherical covariance function given by $\rho(x) = (1 - 3||x||_2/2C + (||x||_2^3/2C^3)\mathbb{1}_{||x||_2\leq C}, x \in \mathbb{R}^2$ (see Bulinski et al. [2012]).

Let $\{Y(x; a, b, \theta); x \in \mathbb{R}^2\}$, be a random field equal in distribution to $\{X(Ax); x \in \mathbb{R}^2\}$ (see Cabaña [1987], Berzin [2021]), where

$$A := \begin{pmatrix} a & 0 \\ 0 & b \end{pmatrix} \begin{pmatrix} \cos(\theta) & \sin(\theta) \\ -\sin(\theta) & \cos(\theta) \end{pmatrix} \tag{13}$$

with $a, b \in \mathbb{R}^2$ and $\theta \in [0, \pi)$. The field Y is also Gaussian with covariance function given by $\rho_Y(x) = (1-3||Ax||_2/2C + (||Ax||_2)^3/2C^3)\mathbb{1}_{||Ax||_2\leq C}$. Note that $a \neq b$ if and only if Y is anisotropic. Initially, we chose to illustrate the computations of the statistics of the oriented perimeter, using this covariance structure with the values $\theta = 0$ and $a = 1$, we then consider different values for θ. Using this model, we implement numerical experiments to validate theoretical results proven in the previous section. We will start with the first moment (see

Figure 7) and second moment (see Figure 8), each time comparing the theoretical result with the empirical one, and then we will proceed to apply the test for different parameters of the affine model above (Figures 9, 10, and Figure D.2 in the supplementary material). Figure 7 is a plot of the value of $\mathbb{E}\left(f^{(2)}(t)\right)$ for $t \in [-3, 3]$, we compare the theoretical curve Equation (3) with the empirical one for different values of b. The increase of the value of b decreases the dependence between the cells in direction 2 which increases the value of $\mathbb{E}\left(f^{(2)}(t)\right)$, as it is shown by Figure D.1 in the supplementary material.

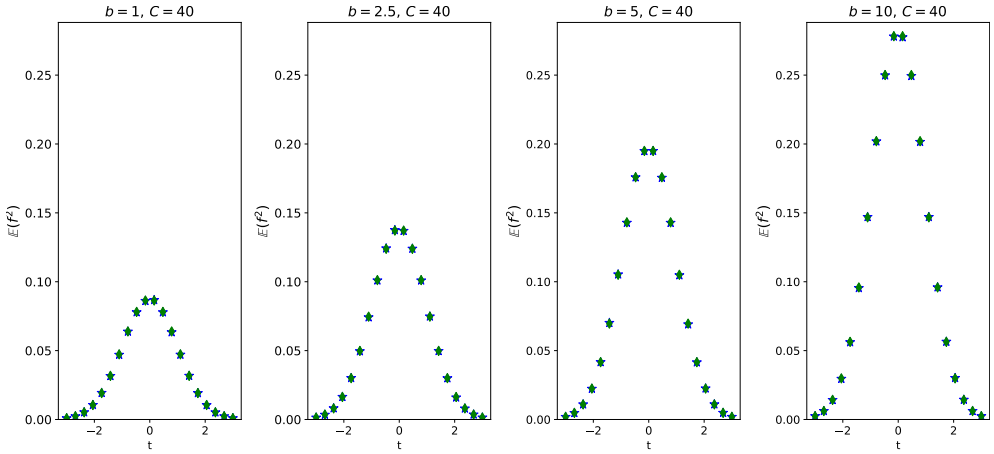

Figure 7: In each panel, we represent the values of $\mathbb{E}\left(f^{(2)}(t)\right)$ in Equation (3) computed for different values of b as a function of the threshold t. The theoretical result is depicted using green diamonds and the empirical values are in blue stars. The computations were done with a Monte-Carlo = 100000, different values of $b = 1, 2.5, 5, 10$ and $C = 40$.

Figure 8 represents the second moment of the perimeter in Equation (10) for different values of C. Recall that C is the length of the compact support of the covariance function ρ (*i.e.*, the bigger the value of C the stronger the dependence in the field). We observe in Figure 8 that the second moment of the perimeter is an increasing function of C. One can add that the variance is maximal for the values $t = -1$ and $t = 1$ and reaches a local minimum on $t = 0$. Furthermore, in Figure 8 (right panel) the empirical variances are computed using the Monte-Carlo method (blue stars) and sub-window method (red crosses). More precisely, regarding the estimation of $\widehat{\sigma}^{(2)}_{M_m,m}(t)$, in this particular context of covariance function with compact support, we consider the constant $C \in \mathbb{R}$ such that $\mathrm{Cov}\left(X_x, X_y\right) = 0$ if $d\left(x, y\right) > C$. Let $\left(V_m^{(i,j)}\right)_{1 \leq i,j \leq M_m}$ be a cutting of the window S such that $\cup_{1 \leq i,j \leq M_m} V_m^{(i,j)} \subset S_m$ and that for $(i, j) \neq (i', j')$, $d\left((i, j), (i', j')\right) > C$, we then compute the ratio $R_{m,i}(t)$ on each sub-window $V_m^{(i,j)}$ and consider the empirical estimator

of the variance over $(R_{m,i}(t))_{1\leq i,j\leq M_m}$ to get $\widehat{\sigma}^{(2)}_{M_m,m}(t)$.

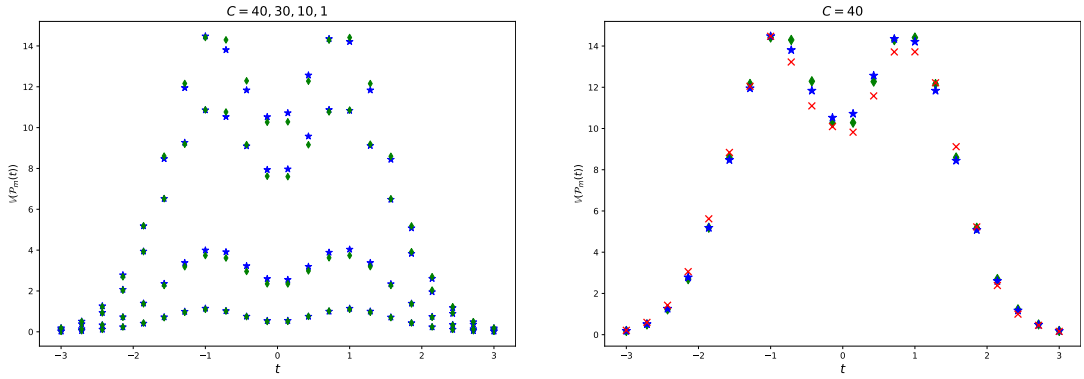

Figure 8: In the left panel, we represent the theoretical values of $\mathbb{V}\left(\frac{1}{m}\mathcal{P}_m(t)\right)$, $m = 512$ from Equation (10) in green (diamonds) and the Monte-Carlo empirical values $\widehat{\sigma}^{(1)}_{n,m}(t)$ in blue (stars). We consider here Monte-Carlo $= 100000$ to compute the theoretical values and Monte-Carlo $n = 2000$ to compute the empirical ones. We set $b = 1$ and from top to bottom $C = 40, 30, 10, 1$. In the right panel, we consider again $C = 40$ and add the estimation of the variance by using the sub-window method (red crosses), $\widehat{\sigma}^{(2)}_{M_m,m}(t)$, the computations were done using an image of size $m = 4800$ and the size of V_i equal 240×240. Here we set $b = 1$ and $C = 40$.

4.2 Numerical studies of local isotropy test

To illustrate the behavior of the test, we chose to rely on two methods computing $\mathbb{P}_{H_0}(\widehat{\phi}_m(t) = 1)$ for H_0 and the p_{value} for H_1 (see Figure 9 and Figure 10) for $b = 1$ and $b = 1.5$ and for $C = 40$ and $C = 20$. The variance of the CLT Formula (7) is estimated using the two methods Monte-Carlo (Figure 9) and sub-window (Figure 10). Under H_0, we plot the values of $\mathbb{P}_{H_0}(\widehat{\phi}_m(t) = 1)$, they range from 0.04 and 0.06 and for H_1 the average value of the p_{value} is $< 10^{-4}$. We also explore the behavior of the test in a more constrained setting (less image data for the Monte-Carlo method and an image of smaller size for the sub-window method). The small size of the patch forces us to restrain the study to threshold levels that are in the neighborhood of 0. That would ensure that one can find observations of the excursion set. Notice that the level $t = 0$ is the global maximum of the expected oriented perimeter (see Figure 7) and a local minimum of the variance (see Figure 8), which makes it the optimal level to consider for inference purposes.

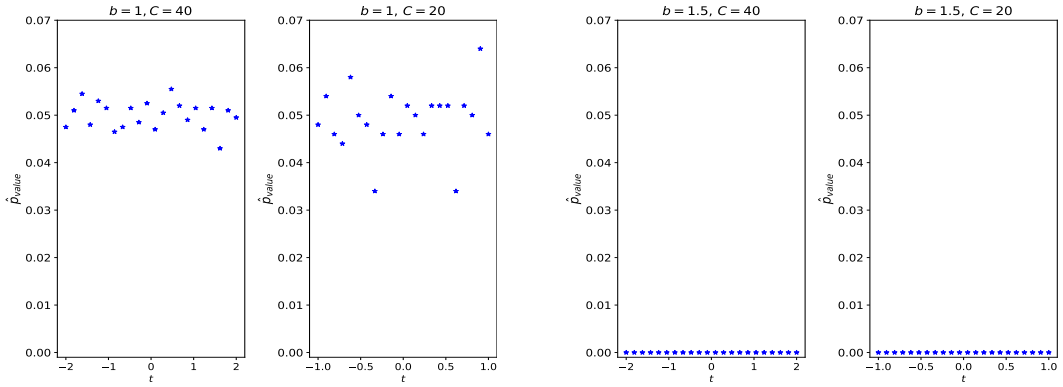

(a) Under H_0 : $\mathbb{P}_{H_0}(\widehat{\phi}_m(t) = 1)$ (b) Under H_1 : $\widehat{p}_{\text{value}}$

Figure 9: We represent the value of $\mathbb{P}_{H_0}(\widehat{\phi}_m(t) = 1)$, (panel (a)) and the $\widehat{p}_{\text{value}} = \frac{1}{n}\sum_{i=1}^{n} 2\mathbb{P}\left(\mathcal{N}(0,1) \geq |z_i|\right)$ with $z_i = \frac{R_{m,i}(t)-1}{\sqrt{\widehat{\sigma}^{(1)}_{n,m}(t)}}$ (panel (b)). The variance $\widehat{\sigma}^{(1)}_{n,m}(t)$ is computed using the Monte-Carlo estimator of the variance by considering for the first and third image starting from the left $n = 2000$ images of size $m = 512$ and $C = 40$ and $t \in [-2, 2]$. For the second and fourth we consider $n = 500$ images of size $m = 512$, $C = 20$ and $t \in [-1, 1]$, $b = 1$ for H_0 and $b = 1.5$ for H_1.

We also present a statistical comparison with the non-parametric test based on the sample variogram proposed by Guan et al. [2004] (see Appendix E). In the following table we present the $\widehat{p}_{\text{value}}$ of the test computed using the Monte-Carlo estimator of the variance (*i.e.* $\widehat{\sigma}^{(1)}_{n,m}(t)$) by considering $n = 2000$ images of size $m = 512$, for critical values of $b = 1.1$ and $b = 1.2$, $C = 40$ and several levels in $[-2, 2]$.

b \ t	-2	-1	-0.5	0	0.2	0.5	1	2
1.1	0.04	$< 10^{-4}$	$< 10^{-4}$	$< 10^{-4}$	$< 10^{-4}$	$< 10^{-4}$	$< 10^{-4}$	0.04
1.2	0.0001	$< 10^{-4}$	$< 10^{-4}$	$< 10^{-4}$	$< 10^{-4}$	$< 10^{-4}$	$< 10^{-4}$	0.0002

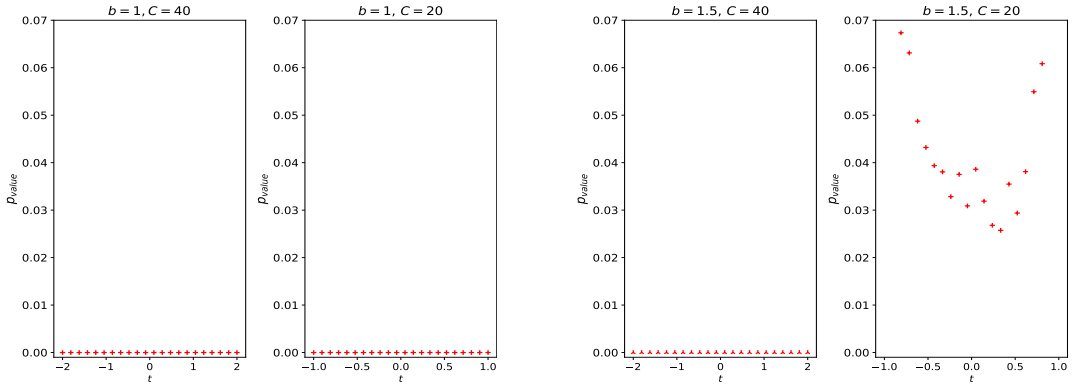

(a) Under H_0 : $\mathbb{P}_{H_0}(\widehat{\phi}_m(t) = 1)$ (b) Under H_1 : $\widehat{p}_{\text{value}}$

Figure 10: We represent the value of $\mathbb{P}_{H_0}(\widehat{\phi}_m(t) = 1)$, (panel (a)) and the $\widehat{p}_{\text{value}} = \frac{1}{n}\sum_{i=1}^{n} 2\,\mathbb{P}\left(\mathcal{N}(0,1) \geq |z_i|\right)$ with $z_i = \frac{R_{m,i}(t)-1}{\sqrt{\widehat{\sigma}^{(1)}_{n,m}(t)}}$ (panel (b)). The variance $\widehat{\sigma}^{(2)}_{M_m,m}(t)$ is computed using the sub-window method by considering for the first and third image starting from the left one single image of size $m = 4800$ and $M_m = 240$ for $C = 40$ and $t \in [-2, 2]$. Finally, for the second and fourth, we consider $m = 1024$ and $M_m = 32$ for $C = 20$ and $t \in [-1, 1]$, $b = 1$ for H_0 and $b = 1.5$ for H_1. For the panel (a) we considered a Monte-Carlo $n = 100$.

We also explore the robustness of our test procedure with respect to the choice of angle θ, see Figure D.2 in Appendix. The results are similar to those presented in Figure 9. However, it is important to note that we only test a form of local isotropy, with preferential axis (e_1, e_2). There exist anisotropic models where $\rho(e_1) = \rho(e_2)$. This is the case of our Gaussian affine model when considering $\theta = \pi/4$. In Figure 11 we see that the proposed test accepts the H_0 hypothesis, which amounts to a type II error.

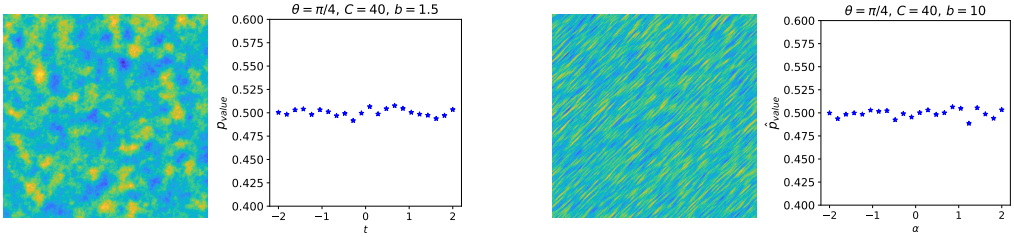

Figure 11: We represent two generations of an affine Gaussian random fields with covariance of a compact support $\rho(x) = (1-3||Ax||_2/2C+(||Ax||_2)^3/2C^3)\mathbb{1}_{||Ax||_2<C}$, as in (13) with $m = 512$, $\theta = \pi/4$, $C = 40$ and $b = 1.1$ (first panel) and $b = 10$ (third panel) respectively. We also display $\widehat{p}_{\text{value}} = \frac{1}{n}\sum_{i=1}^{n} 2\mathbb{P}\left(\mathcal{N}(0,1) \geq |z_n|\right)$ with $z_i = \frac{R_{m,i}(t)-1}{\sqrt{\widehat{\sigma}^{(1)}_{n,m}(t)}}$ in blue color computed for a Monte-Carlo $n = 2000$, for $b = 1.5$ (second panel) and $b = 10$ (fourth panel).

5 Local isotropy test on bone X-rays

Description of the considered bone X-rays. The studied X-ray images were acquired at INSERM U658 (Orleans, France) using a standardized procedure Lespessailles et al. [2007, 2008]. They were obtained on the calcaneus (a heel bone) with a direct digital X-ray prototype (BMA$^{\text{TM}}$, D3A Medical Systems, Orleans, France) with focal distance 1.15 m and X-ray parameters 55 kV and 20 mAs. The high-resolution digital detector integrated into the device prototype had a 50 μm pixel size, providing a spatial resolution of 8 line pairs per millimeter at 10% modulation transfer function. For each subject, the software device selected a region of interest (ROI) of constant size 400×400 pixels corresponding at a same position using three predefined anatomical landmarks localized by the operator (see Figure 12). The database contains radiographs of 211 post menopausal women, 165 being control cases and 46 osteoporotic fracture cases and was previously studied in Biermé et al. [2009].

We first applied a pre-processing step in order to get stationary images. This step is performed by subtracting the trend which is represented by a plane obtained via a mean-square linear regression. Furthermore, to avoid boundaries issues, we decided to crop from a 400×400 image to a 380×380 image. It is also necessary to standardize the images to be in the centered and unit variance framework, considered in this work.

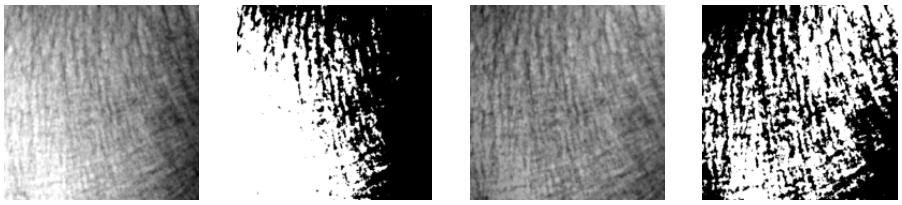

Figure 12: Example of images before (first panel) and after (third panel) the stationary procedure and their excursion sets at quantile level $\alpha = 0.5$ (second and four panels, respectively).

A quick word regarding the choice of the threshold. To insure that the images of two excursion sets can be compared, we chose to select the threshold as quantile levels of the image. This method imposes a geometrical constraint on the choice of the threshold level, which guaranties the comparability of the excursion sets. Thus for an image X, for $\alpha \in (0, 1)$ the considered threshold is $t_\alpha = \widehat{F}_X^{-1}(\alpha)$ with $\widehat{F}_X$ the empirical cumulative distribution function of the image X. After this pre-processing, Figure 2 suggested the

existence of two clusters in regard to the ratio of the two perimeters. Indeed, we observe a cluster of points for which the ratio $\mathcal{P}_1(t_\alpha)/\mathcal{P}_2(t_\alpha) < 1$. This means that the corresponding images are mis-oriented. Thus, before proceeding further with the local isotropy test, we apply a second pre-processing step: a $\pi/2$-rotation to these specific images. The new obtained boxplots are gathered in Figure 13.

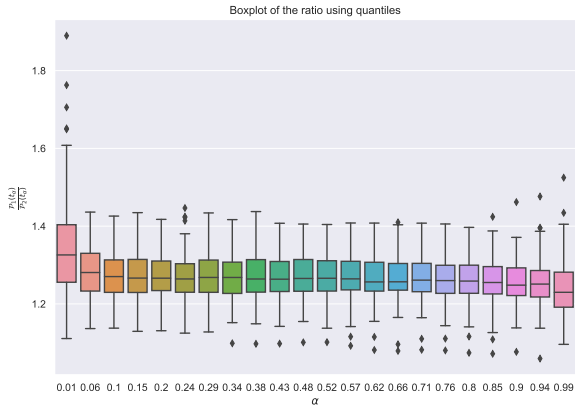

Figure 13: For $\alpha \in [0.01, 0.99]$, we represent the boxplot of the ratios $(R_{m,i}(t_\alpha))_{i\leq 211}$, with $R_{m,i}(t_\alpha) = \mathcal{P}^{(1)}_{m,i}(t_\alpha)/\mathcal{P}^{(2)}_{m,i}(t_\alpha)$ at t_α level with $t_\alpha = \widehat{F}^{-1}_X(\alpha)$, for bone X-rays after pre-processing stationary step and rotation, when necessary.

Applying the local isotropy test. We can now proceed to the local isotropy test. To this aim, we compute $p_{\text{value},i}(t_\alpha) = 2\mathbb{P}\left(\mathcal{N}(0,1) > |R_i(t_\alpha) - 1)|\,/\widehat{\sigma}^{(1)}_{211,380}(t_\alpha)\right)$, for each image X_i with the Monte-Carlo estimated variance $\widehat{\sigma}^{(1)}_{211,380}(t_\alpha)$ (see Section 3.3) and then we represent $\widehat{p}_{\text{value},211} = \frac{1}{211}\sum_{i=1}^{211} p_{\text{value},i}(t_\alpha)$ in Figure 14.

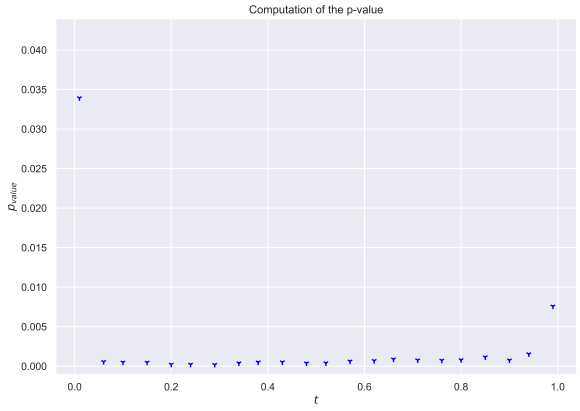

Figure 14: For $\alpha \in [0.01, 0.99]$, we represent the p_{value} of the test computed for different levels t_α for stationary thresholded and eventually rotated images of bone X-rays.

As expected the result of the hypothesis test $\widehat{p}_{\text{value}} < 0.05$ indicates that the data exhibit anisotropy, this leads us to reject the hypothesis of local isotropy. Furthermore, when

analyzing Figure 13, the distribution of the ratio $(R_{m,i}(t))_{i\leq n}$ seems to be invariant in regards to the threshold level, as already noticed in Remark 2. This suggests that the field is highly dependent. In order to corroborate this intuition, we estimate $\rho(e_i)$ by applying Proposition 3.3 and using the total variation of the image. Figure 15 confirms the highly local dependence behavior of the considered images, *i.e* $\widehat{\rho}_i(e_j) \approx 1$ for $j = 1, 2$ and $1 \leq i \leq 211$.

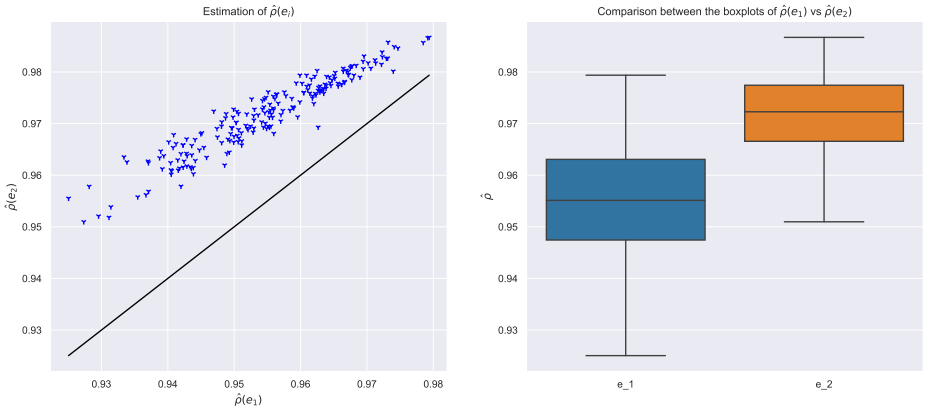

Figure 15: In the left panel, we represent the couple $(\widehat{\rho}_i(e_1), \widehat{\rho}_i(e_2))$ for each image X_i. On the right panel, we represent the boxplot of $(\widehat{\rho}_i(e_1))_{i\leq 211}$ (blue) and $(\widehat{\rho}_i(e_2))_{i\leq 211}$ (orange).

6 Conclusion and discussion

In this paper, we have introduced a novel statistical technique for evaluating the local isotropy property of a Gaussian random field. By utilizing the oriented perimeter of the excursion set, we were able to build a consistent test based only on this sparse observation. We also successfully applied the test to real world data to test the anisotropic nature of bone texture. As we have seen above, the proposed test does not require any prior knowledge of the field, however, it performs best when the selected threshold is close to the mean value of the field and worse for extreme levels t. One potential improvement would be to study the behavior of the ratio between the first and second moment of the oriented perimeter in a dense tiling framework. If an equivalence between the two is established, it would short cut the inference of the variance, using the first moment instead, and hopefully increasing the performance of the test for extreme thresholds. Finally, we obtained a closed form for both the first and second moments which renders possible a thorough study of the infill framework (*i.e.* $\rho(e_i) \to 1$), which yields a shift from the discrete setting to the continuous one.

References

M. Abaach, H. Biermé, and E. Di Bernardino. Testing marginal symmetry of digital noise images through the perimeter of excursion sets. *Electronic Journal of Statistics*, 15(2): 6429 – 6460, 2021.

M. A. Arcones. Limit theorems for nonlinear functionals of a stationary gaussian sequence of vectors. *The Annals of Probability*, 22(4):2242–2274, 1994.

C. Berzin. Estimation of local anisotropy based on level sets. *Electronic Journal of Probability*, 26:1–72, 2021.

H. Biermé and A. Desolneux. The effect of discretization on the mean geometry of a 2D random field. *Annales Henri Lebesgue*, 4:1295–1345, 2021.

H. Biermé, F. Richard, and C. L. Benhamou. Parametric estimation for Gaussian operator scaling random fields and anisotropy analysis of bone radiograph textures. In K. Pohl, editor, *International Conference on Medical Image Computing and Computer Assisted Intervention MICCAI'09*, pages 13–24, London, France, 2009.

H. Biermé, E. Di Bernardino, C. Duval, and A. Estrade. Lipschitz-Killing curvatures of excursion sets for two-dimensional random fields. *Electronic Journal of Statistics*, 13(1), 2019.

A. Bulinski, E. Spodarev, and F. Timmermann. Central limit theorems for the excursion set volumes of weakly dependent random fields. *Bernoulli*, 18(1):100 – 118, 2012.

E. M Cabaña. Affine processes: a test of isotropy based on level sets. *SIAM Journal on Applied Mathematics*, 47(4):886–891, 1987.

C. Chappard, B. Brunet-Imbault, G. Lemineur, B. Giraudeau, A. Basillais, R. Harba, and C. L. Benhamou. Anisotropy changes in post-menopausal osteoporosis: characterization by a new index applied to trabecular bone radiographic images. *Osteoporosis International*, 16:1193–202, 2005.

E. Di Bernardino and C. Duval. Statistics for Gaussian random fields with unknown location and scale using Lipschitz-Killing curvatures. *Scandinavian Journal of Statistics*, pages 1–42, 2020.

E. Di Bernardino, A. Estrade, and J. R. León. A test of Gaussianity based on the Euler Characteristic of excursion sets. *Electronic Journal of Statistics*, 11(1):843–890, 2017.

Yongtao Guan, Michael Sherman, and James A Calvin. A nonparametric test for spatial isotropy using subsampling. *Journal of the American Statistical Association*, 99(467): 810–821, 2004.

E. Lespessailles, C. Gadois, G. Lemineur, J. P. Do-Huu, and C. L. Benhamou. Bone texture analysis on direct digital radiographic images: precision study and relationship with bone mineral density at the os calcis. *Calcif. Tissue Int.*, 80:97–102, 2007.

E. Lespessailles, C. Gadois, I. Kousignian, J. P. Neveu, P. Fardellone, S. Kolta, C. Roux, J. P. Do-Huu, and C. L. Benhamou. Clinical interest of bone texture analysis in osteoporosis: a case control multicenter study. *Osteoporosis International*, 19:1019–28, 2008.

M. S Longuet-Higgins. The statistical analysis of a random, moving surface. *Philos. Trans. Roy. Soc. London Ser. A*, 249:321—-387, 1957.

MATLAB. *Update 4 (9.9.0.1570001) (R2020b)*. The MathWorks Inc., Natick, Massachusetts, 2021.

A. Molina and F. R. Feito. A method for testing anisotropy and quantifying its direction in digital images. *Computers & Graphics*, 26(5):771–784, 2002.

F.J.E. Telschow, A. Schwartzman, D. Cheng, and P. Pranav. Estimation of Expected Euler Characteristic Curves of Nonstationary Smooth Gaussian Fields. *arXiv preprint arXiv:1908.02493*, 2020.

I.M. Wani and S. Arora. Computer-aided diagnosis systems for osteoporosis detection: a comprehensive survey. *Medical and Biological Engineering and Computing*, 58:1873–1917, 2020.

Zachary D. Weller and Jennifer A. Hoeting. A Review of Nonparametric Hypothesis Tests of Isotropy Properties in Spatial Data. *Statistical Science*, 31(3):305 – 324, 2016.

K. J. Worsley. The geometry of random images. *Chance*, 9(1):27–40, 1996.